

Natural and artificial aging behaviour of Al-Cu-Mg-Ag-Ti-B (A205) alloy processed by laser powder bed fusion: Strengthening mechanisms and failure analysis

Original

Natural and artificial aging behaviour of Al-Cu-Mg-Ag-Ti-B (A205) alloy processed by laser powder bed fusion: Strengthening mechanisms and failure analysis / Barode, Jayant; Vayyala, Ashok; Aversa, Alberta; Yang, Luyan; Mayer, Joachim; Fino, Paolo; Lombardi, Mariangela. - In: MATERIALS TODAY COMMUNICATIONS. - ISSN 2352-4928. - 39:(2024), pp. 1-14. [10.1016/j.mtcomm.2024.108978]

Availability:

This version is available at: 11583/2989305 since: 2024-06-04T13:28:10Z

Publisher:

Elsevier

Published

DOI:10.1016/j.mtcomm.2024.108978

Terms of use:

This article is made available under terms and conditions as specified in the corresponding bibliographic description in the repository

Publisher copyright

(Article begins on next page)



Natural and artificial aging behaviour of Al-Cu-Mg-Ag-Ti-B (A205) alloy processed by laser powder bed fusion: Strengthening mechanisms and failure analysis

Jayant Barode^{a,*}, Ashok Vayyala^b, Alberta Aversa^a, Luyan Yang^{b,d}, Joachim Mayer^{b,c}, Paolo Fino^a, Mariangela Lombardi^a

^a Department of Applied Science and Technology, Politecnico Di Torino, Corso Duca degli Abruzzi 24, Torino 10129, Italy

^b Ernst Ruska-Centre for Microscopy and Spectroscopy with Electrons (ER-C-2), Forschungszentrum Jülich GmbH, Jülich 52425, Germany

^c Central Facility for Electron Microscopy (GFE), RWTH Aachen University, Ahornstr. 55, Aachen 52074, Germany

^d Beijing Key Lab of Microstructure and Properties of Advanced Materials, Faculty of Materials and Manufacturing, Beijing University of Technology, Beijing 100124, China

ARTICLE INFO

Keywords:

LPBF
Aluminium alloys
Post-processing
Strengthening mechanisms

ABSTRACT

The Al-Cu-Mg-Ag-Ti-B (A205) alloy has gained success in the additive manufacturing domain due to its good processability. It is a precipitation hardening alloy, and because of this, its mechanical properties are greatly influenced by post-processing treatments. In the present work, A205 samples processed by laser powder bed fusion were first solution treated and then aged by: (i) natural aging (NA) and (ii) artificial aging (AA). The effects of different aging treatments on the microstructure and mechanical behaviour were evaluated. Both NA and AA heat treatments improved the mechanical behaviour of as-built A205 alloy. Peak hardness was achieved in 20 days (≈ 137 HV) for the NA specimen, whereas it took 4 h at 190°C (≈ 144 HV) for the AA specimen. The average yield strength, ultimate tensile strength and elongation to fracture for NA and AA were, 276 MPa, 434 MPa, 20% and 397 MPa, 463 MPa, 11%, respectively. The structure-property correlation was analysed by evaluating various strengthening factors. Considerable grain boundary strengthening was observed in both NA and AA specimen. The major strengthening contributions in the NA specimen were due to the disordered Ag-Mg co-clusters and solid solution strengthening by Cu. In AA instead, strengthening due to the precipitation of plate-type Ω/θ' - Al_2Cu phase was dominant. In the end, failure mechanisms in the NA and AA conditions were also briefly discussed. The laser powder fused A205 alloy demonstrated a significant response to the NA and possessed a high-ductility and good-strength combination.

1. Introduction

Laser powder bed fusion (LPBF) is a cutting-edge additive manufacturing technology. It has emerged as a groundbreaking method for creating intricate and fully dense metallic components with exceptional precision and structural integrity [1]. It utilizes a high-power laser to selectively melt and fuse layers of powdered metal. LPBF adaptability extends to various metallic alloys, including stainless steels [2], Ti alloys [3], Al alloys [4], Ni-based superalloys [5]. However, LPBF of high strength Al alloys is generally challenging for two main reasons (i) high tendency to hot cracking and (ii) high laser reflectivity under fibre laser ($\lambda \approx 1.06 \mu\text{m}$) [4,6]. These issues have greatly limited the range of high

strength Al alloys that can be successfully processed by LPBF [6]. Recently, a new high strength Al alloy-A20XTM developed by Aeromet International Limited has overcome the limitations of both hot cracking tendency and high laser reflectivity [7–9]. The company took the advantage of TiB_2 particles embedded within the powder particle matrix which significantly improved their laser absorptivity [10,11], and also promoted the formation of equiaxed grains during solidification in the LPBF process [12]. Equiaxed grains are more strain tolerant than columnar ones and thus reduces the tendency to hot cracking [12,13]. Apart from acting as a grain refiner, TiB_2 particles also contributes to the strengthening of an alloy by various mechanisms such as load bearing, Orowan strengthening, modulus mismatch strengthening and due to the

* Corresponding author.

E-mail address: jayant.barode@polito.it (J. Barode).

<https://doi.org/10.1016/j.mtcomm.2024.108978>

Received 10 January 2024; Received in revised form 26 February 2024; Accepted 18 April 2024

Available online 20 April 2024

2352-4928/© 2024 The Authors. Published by Elsevier Ltd. This is an open access article under the CC BY license (<http://creativecommons.org/licenses/by/4.0/>).

difference in the coefficient of thermal expansion (CTE) [14–16].

The A20X™ powders were derived from A205 alloy which is an Al-Cu-Mg-Ag-TiB₂ system [17]. In this alloy Cu and Mg are responsible for the precipitation of strengthening phases such as θ' -Al₂Cu (high Cu/Mg ratio) and S' -Al₂CuMg (low Cu/Mg ratio) phases [18]. Besides Cu and Mg, the addition of Ag promotes the formation of Ag-Mg co-clusters in the early stages of aging [19–23]. The Ag-Mg co-clusters act as a precursor to the precipitation of Ω -Al₂Cu phase [24–28]. Ω possesses a plate-type morphology and a similar chemical composition (Al₂Cu) as θ' [25,29]. Although Ω prefers to nucleate on the {111} Al while θ' on {001} [25,30,31]. Both Ω and θ' are considered as major strengthening phases in an A205 alloy [15,30,32,33]. Being an obstacle to the dislocation motion on Al primary glide plane i.e. {111}, Ω offers much higher strength than θ' [34–36].

In the recent past, there have been multiple studies on the LPBF processing behaviour of A205 alloy [15,37–40]. The LPBF-A205 alloy can be easily processed with a crack-free and a near fully dense microstructure [37,38]. The as-built state has a cellular microstructure with equiaxed grains/cells and no preferential crystallographic orientation. The cell boundaries were identified as eutectic θ -Al₂Cu [37,39]. The TiB₂ particles were uniformly distributed across the sample [41]. The as-built state demonstrated isotropic tensile properties but were also accompanied by the formation of Lüders band and serrated flow behaviour (Portevin-Le Chatelier (PLC) effect) in the plastic regime, such a behaviour was associated to the trapping of solute atoms (particularly Mg) at the substitutional sites in the Al lattice during LPBF processing [39]. Since A205 is a precipitation hardening alloy, much attention has been given to the development of the post-processing heat treatments [15,16,30,32,33,42]. For example, Shakil et al. [16] and Avateffazeli et al. [32] performed a modified T7 post-processing heat treatment, which comprises of a two-step solutioning (505°C for 2 h + 530°C for 4 h) followed by artificial aging at 190°C for 4–6 h. It was reported that T7 significantly improved the yield strength (43%) and ultimate tensile strength (38%) with respect to the as-built condition. The increased strength was attributed to the precipitation of nano-sized plate-type Ω - and θ' -Al₂Cu precipitates, however, the ductility was decreased by 24%. Jiang et al. modified the two-step solutioning stages to 513°C for 2 h + 527°C for 10 h followed by artificial aging at 180°C for 16 h and reported a good combination of a high strength (405 MPa) and ductility (11.6%) [15]. A similar combination of strength and ductility could also be achieved with only one-step solutioning (530°C for 1 h) and then aged at 190°C for 6 h [30] or at 180°C for 10 h [42]. Besides artificial aging, another promising heat treatment is natural aging (solutioning followed by room temperature aging) [43–45]. Zuiko et al. [46] reported that a long-term natural aging (2 months) offers a good combination of strength and ductility in a casted Al-Cu-Mg alloy. Chen et al. [45] observed that natural aging of 24 h allowed the formation of Ag-Mg co-clusters that improved the precipitation kinetics of Ω phase during artificial aging in a casted Al-Cu-Mg-Ag alloy. Furthermore, it was observed that Ag-Mg co-clusters could also be utilized as a strengthening factor [23,43,44,47]. Ünlü et al. [43] observed an increase in hardness of ≈ 40 H_{RB} in a casted Al-5Cu-0.5Mg-0.4Ag (wt%) alloy after natural aging for 7 days. This increase was associated to the formation of Ag-Mg co-clusters. Weng et al. [44] also reported a hardness increment of ≈ 8 HV from 2 days of natural aging up to 14 days in a casted Al-0.71Si-1.13Mg-0.49Ag alloy. Natural aging also has been reported to influence the precipitation process during subsequent artificial aging [48,49]. Thus, an understanding of the behaviour of an LPBF A205 alloy under natural aging is crucial in order to design new heat treatments that are economically viable but also improve the properties of the printed parts.

To the best of our knowledge, no literature has so far reported on the natural aging behaviour of the A205 alloy processed by LPBF. In the present investigation, a comparative study of two post-processing conditions i.e., natural and artificial aging behaviour is presented by the combined analysis of microstructural, thermal, and mechanical

characterizations along with understanding the fracture behaviour. Furthermore, a structure-property correlation has been established by quantitatively evaluating various strengthening mechanisms arising from grain boundaries, solid solution, TiB₂ particles, precipitates, and atomic clusters in these two post-processing conditions as well as in the as-built state.

2. Material and methods

A commercial gas atomized A205 (A20X™) powder with embedded pre-existent TiB₂ particles was purchased from ECKART GmbH. A SEM micrograph of the powder is provided in Fig. 1a and the nominal composition of the powder, provided by the supplier, is presented in Table 1. The detailed analysis of the powder characterization has been presented in our previous work [30]. The powders were mostly spherical in shape with few satellite particles. The particle size distribution displayed a unimodal distribution with D₁₀, D₅₀ and D₉₀ as 21 μ m, 30.6 μ m and 49.8 μ m, respectively. Cubic samples (10 \times 10 \times 10 mm³) were printed by LPBF process using an EOS M270 dual mode system (Fig. 1b). The printing process was performed in an argon atmosphere, platform was pre-heated to 100°C and a scanning strategy of rotating 67° stripes was used.

The optimized printing parameters employed were laser power = 195 W, scan speed = 800 mm/s, hatching distance = 0.13 mm, layer thickness = 30 μ m and a consequent volumetric energy density (VED) = 62.5 J/mm³. The maximum relative density of $\approx 99.93 \pm 0.04\%$ could be achieved. The parameters were optimized based on minimum amount of porosity values while still maintaining the low VED and a high build-up rate. The effect of various processing parameters on porosity can be found in a supplementary file (Fig S1).

Two post-processed heat treatments were performed: (i) natural aging (NA) and (ii) artificial aging (AA).

- (i) NA: Solution treatment at 530°C for 1 h + water quenching + room temperature aging ($\approx 28^\circ$ C). The room temperature here is an average temperature of the total days in which the experiments were performed.
- (ii) AA: Solution treatment at 530°C for 1 h + water quenching + aging at 190°C + air cooling

The solution treatment was performed in a horizontal tubular furnace (Nabertherm RHTC 80–710/15) under an argon atmosphere. The artificial aging treatment was performed in an oven (Memmert) for different aging time (up to 30 h). Natural aging was done for various number of days (up to 100) at room temperature.

Metallographic sample preparations were performed by polishing according to the standard metallographic procedure. Peak aged conditions in NA (T4) and AA (T6), termed as NA-20d and AA-4 h were considered for the further microstructural characterization. Microstructural characterizations were performed using an optical microscope (Leica DMI 5000 M), a Phenom XL table-top scanning electron microscope (SEM) equipped with secondary electron (SE), back scattered electron (BSE) detectors and an energy dispersive spectroscopy (EDS). Electron backscattered diffraction (EBSD) was performed in a TESCAN S900 field emission scanning electron microscope (FESEM) using 20 kV and 10 nA with a step size of 0.2 μ m. Transmission electron microscopy (TEM) characterizations were done on a very thin lamella of thickness close to 100 nm. These lamellae were obtained by a site-specific sample preparation technique from bulk samples using Focused Ion Beam (FIB) in a Helios NanoLab 460 F1 dual beam FIBSEM equipped with Ga⁺ ion source. The thickness of the samples was assessed during the final stages of FIB sample preparation, utilizing its precise milling capabilities. A more detailed procedure on such sample preparation technique can be found at [50]. EDS mapping was carried out in an FEI Titan G2 80–200 ChemiSTEM microscope at 200 kV as described in our previous work [30]. The morphological features of the precipitates in an artificial aged

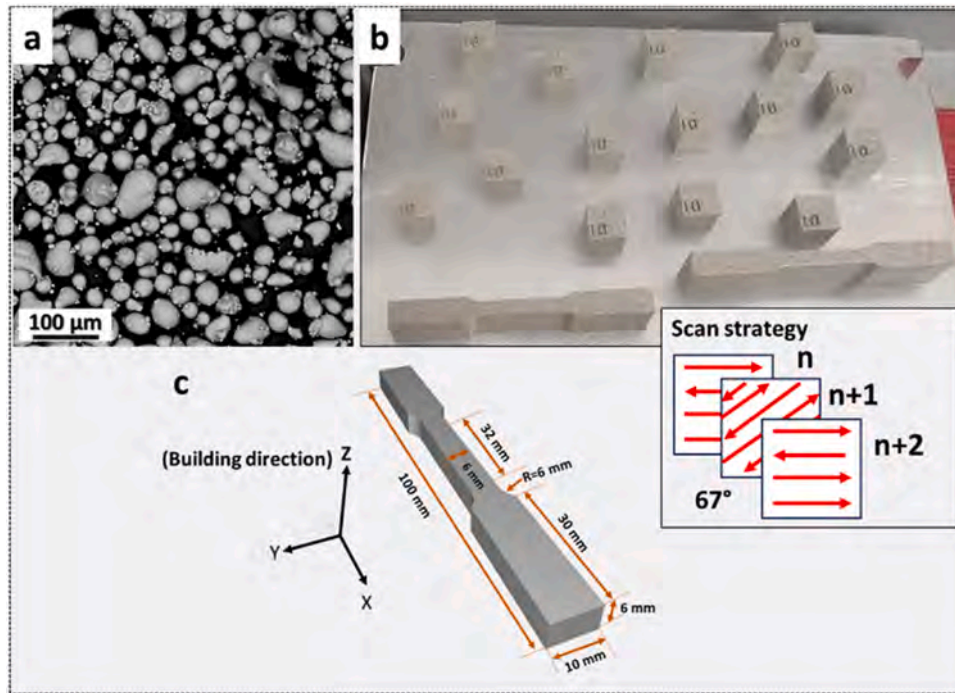


Fig. 1. (a) SEM micrograph of the A20X powder, (b) built platform with printed parts and (c) a schematic of tensile specimen with ASTM E8 dimensions.

Table 1

Chemical composition of A205 powder.

	Cu	Mg	Ag	Fe	Si	Ti	B	Al
wt%	4.2–5.0	0.2–0.33	0.60–0.90	<0.1	<0.1	3.0–3.8	1.25–1.55	Balance

specimen were quantified by ImageJ 1.53 k software [51]. Their volume fraction (f_v) and number density per unit volume (n) were calculated from the TEM micrographs by the Nei and Muddle method [34,52]:

$$n = \frac{N_1 + N_2}{A_{\text{Obs}} \times (T + d_t)} \quad (1)$$

$$N_2 = N_1 \times \frac{T + d_t}{\sqrt{A_{\text{Obs}}}} \quad (2)$$

$$f_v = n t_t \times \frac{(\pi d_t^2)}{4} \quad (3)$$

Where N_1 is the number of precipitates observed, N_2 is the number of precipitates not visible, due to weak contrast and overlapping of precipitates in the same region, A_{Obs} is the area of the observed region, T is the foil/lamella thickness, t_t and d_t are the average precipitate thickness and diameter, respectively.

Phase analysis was carried out by X-ray diffraction (XRD) in a Panalytical X'Pert PRO PW 3040/60 X-ray diffractometer using a monochromatic $\text{Cu-K}\alpha$ radiation of 1.54 \AA operated at 40 kV and 40 mA with a step size of 0.013° and 25 s. per step and 0.007° and 50 s. per step for the whole and individual peak profiles, respectively. Instrumental broadening was obtained from the spectrum of LaB_6 standard sample. Dislocation density was calculated by XRD line profile analysis using the Williamson-Hall (W-H) plot [24,25]. Differential scanning calorimetry (DSC) curves were obtained using NETZSCH 214 Polyma. DSC samples were heated from 25°C to 570°C at $20^\circ\text{C}/\text{min}$ in a N_2 atmosphere. The baseline was corrected by the NETZSCH Proteus software and subtracted with Origin 8.5 software. Micro-hardness values were obtained with a micro-Vickers Leica VMHT indenter using 100 g load and 15 s of dwell time (10 measurements/sample). The tensile samples were built parallel

to the base plate according to the ASTM E8 but with a higher thickness. The required thickness for the ASTM E8 was made by the electrical discharge machining (EDM). The dimension of the tensile specimen is presented in a Fig. 1c. Tensile tests were performed by Zwick-Roell ProLine Z0505 with $8 \times 10^{-3} \text{ s}^{-1}$ as strain rate. In total 9 samples were tested, 3 samples for each condition i.e., as-built (AB), NA-20d and AA-4 h.

3. Results

3.1. Micro-hardness response

The micro-hardness evolution of the NA and AA specimens is presented in Fig. 2. There was a rapid increase in the micro-hardness values of AA specimens when aged from the as-quenched state i.e., 0 h to 2 h. The A205 specimens reached their peak hardness value of 144 HV upon 4 h of artificial aging and retained the peak hardness up to 8 h. Aging longer than 8 h, only slightly decreased the hardness.

For the NA, the hardness developed more gradually. The NA sample reached its peak hardness value after 20 days (138 HV). The hardness value remained more or less constant up to 100 days.

3.2. Thermal analysis

The DSC spectra of NA and AA specimens are shown in Fig. 3. The heat flow behaviours at low- and high-temperatures are presented in Fig. 3a and b. Only one endothermic peak was found in the $60\text{--}180^\circ\text{C}$ temperature range (Fig. 3a), which has been associated with the dissolution of Ag-Mg co-clusters [27,30,53,54]. The area under the curve continued to increase as a function of NA time indicating that Ag-Mg co-clusters were formed and have grown during NA. Furthermore, the

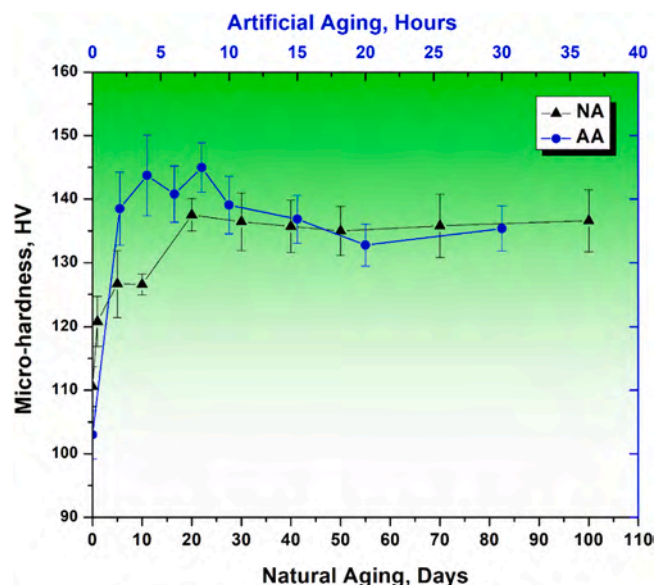


Fig. 2. Micro-hardness evolution as a function of natural and artificial aging time.

peak temperature slightly shifted towards higher temperatures indicating that more stable clusters are being dissolved and suggesting that the mean cluster size increased during aging. No endothermic peak was observed in the case of NA-0 days and AA-4 h specimen (Fig. 3a).

At higher temperatures (180–550°C) (Fig. 3b), two more peaks were observed. First, is an exothermic peak, that corresponds to the precipitation of stoichiometric Al_2Cu in various forms, namely, Ω , θ' and θ as identified in our previous work [30]. The second, is a broad endothermic peak indicating the dissolution of all forms of Al_2Cu precipitates. The dissolution occurred over a wide range of temperatures with its peak around 525°C and thereafter a sharp drop having a peak offset temperature of $\approx 530^\circ\text{C}$. The dissolution peak area and peak temperature were very similar in all the conditions of NA and AA specimens. The peak temperature for the precipitation tends to shift towards higher temperatures after NA-5 days.

3.3. Phase analysis

The peak aged conditions in both naturally aged and artificially aged specimens were considered for further characterizations and from now

on in the manuscript, NA-20d indicates “naturally aged for 20 days” and AA-4 h indicates “artificially aged for 4 h”.

The XRD spectra of NA-20d and AA-4 h are shown in Fig. 4. Their whole line profile in Fig. 4a. Three phases were observed, namely, Al, $\theta\text{-Al}_2\text{Cu}$ and TiB_2 . The reference codes utilized for Al, $\theta\text{-Al}_2\text{Cu}$ and TiB_2 were 98-006-1729 [55], 98-009-6862 [56] and 98-001-3140 [57] of ICDD respectively. The individual peak profile of $\theta\text{-Al}_2\text{Cu}$ {110} and Al {111} planes are presented in Fig. 4b and c, respectively. It was demonstrated in our previous work that single-step solutioning allowed more complete dissolution of eutectic $\theta\text{-Al}_2\text{Cu}$ [30]. The primary {110} peak of $\theta\text{-Al}_2\text{Cu}$ was absent in a NA specimen indicating a more complete dissolution while it appears in the AA-4 h specimen (Fig. 4b). In addition, the AA-4h resulted in a broader Al {111} peak than in the NA-20d specimen. The estimated dislocation density values were calculated based on W-H plot. The average dislocation density in the AA-4h specimen ($4.5 \times 10^{14} / \text{m}^2$) was almost twice to that of in NA-20d ($2.1 \times 10^{14} / \text{m}^2$).

3.4. Microstructure

The microstructural characterization of NA-20d and AA-4 h has been carried out by EBSD (Fig. 5), SEM (Fig. 6) and HAAD-STEM (Fig. 7 and Fig. 8). The EBSD data are reported as inverse pole figure (IPF) maps (Fig. 5a and 5b), phase maps (Fig. 5c and d), grain size distributions (Fig. 5e and f) and distribution of grain boundaries in terms of misorientation angle among random pairs (Fig. 5g and h) based on Mackenzie plot [58]. The high-angle grain boundaries (HAGB) and low-angle grain boundaries (LAGB) are separated by 15° misorientation angle. Both the post-processing conditions revealed an equiaxed and highly isotropic microstructure i.e., no presence of texture (Fig. 5a-b). The average grain size in NA-20d and AA-4 h specimens were $1.98 \mu\text{m}$ and $2.43 \mu\text{m}$, respectively. In both NA-20d and AA-4 h, majority of grain boundaries are of high angle grain boundaries (HAGB), comprising nearly 97.04% and 96.92% respectively. The corresponding phase map distinguished the TiB_2 particles and their distribution. These particles were usually observed at the grain triple junctions and grain boundaries (GBs), some finer- TiB_2 particles were also located inside the grains.

Under the SEM-BSE mode (Fig. 6), the Al-matrix appeared grey, both TiB_2 particles and Al_2Cu phase were observed as white. In the AA-4 h specimen, discontinuous precipitates were observed as white dots at the grain boundaries (Fig. 6b). Such grain boundary precipitates were not observed in the NA-20d specimen (Fig. 6a). It indicates that the solutes that remained within the Al lattice after solutioning did not precipitate during NA, and thus the average concentration of solutes namely, Cu (4.8 ± 0.20), Ag (0.99 ± 0.16) and Mg (0.25 ± 0.05) wt% was obtained

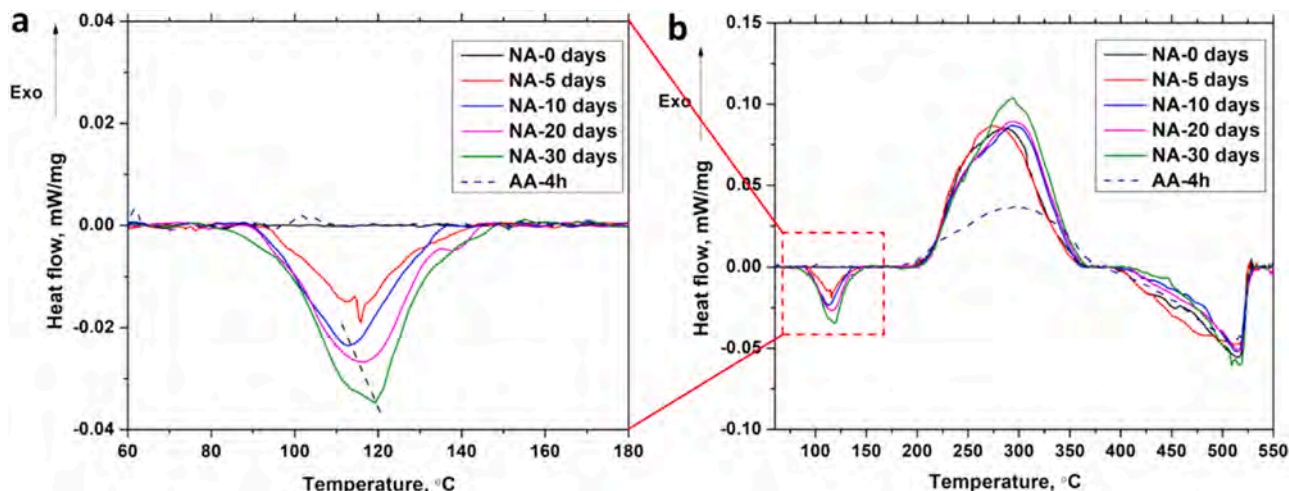


Fig. 3. Heat flow behaviour of NA for various number of days and AA for 4 h in (a) low-temperature and (b) high-temperature range.

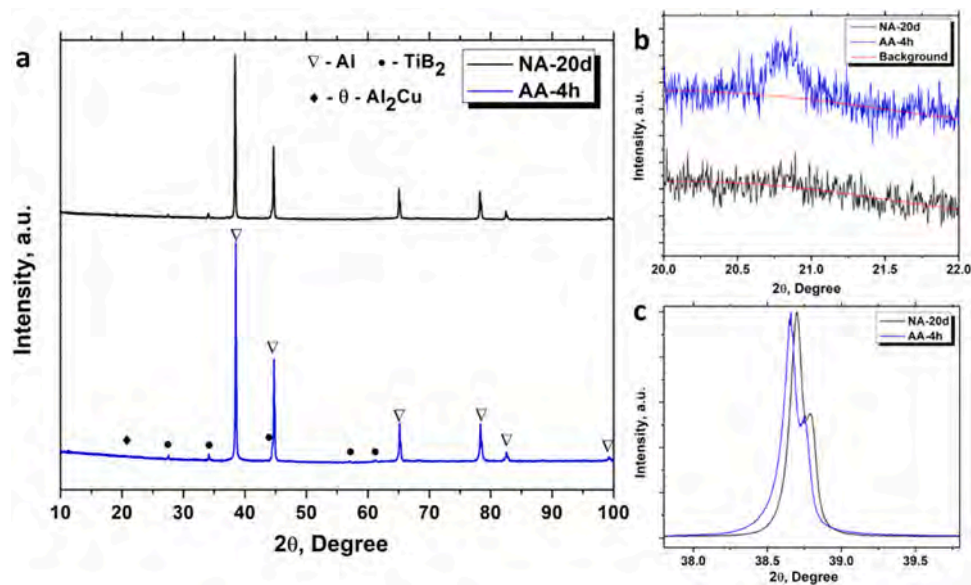


Fig. 4. XRD spectra of NA-20d and AA-4 h showing (a) whole line profile, (b) θ -Al₂Cu {110} and (c) Al {111}.

by performing the EDS spot analysis inside the grains.

Characterizations by a HAAD-STEM are displayed in Fig. 7 and Fig. 8. Low and high magnification micrographs of the NA-20d specimen are shown in Fig. 7a-b. The corresponding EDS maps of Fig. 7a is presented in Fig. 7c-f. Similarly, low and high magnification micrographs of AA-4h specimen are shown in Fig. 8a-b and their corresponding EDS maps in Fig. 8c-f.

Fig. 8a-b confirmed the presence of grain boundary precipitates and precipitates at micro/nano-TiB₂ particles in an AA-4 h specimen. These precipitates are likely to be of an equilibrium θ -Al₂Cu phase (irregular Cu rich phase). Such precipitation leads to the formation of precipitate free zones (PFZs) in their vicinity, as observed in Fig. 8b. In addition, STEM micrographs also revealed the presence of high number density ($\approx 5.05 \times 10^{21}/\text{m}^3$) of plate-type matrix precipitates having an average thickness (t_p) and diameter (d_p) of 1.7 nm and 54 nm, respectively (Fig. 8b). These plate-type precipitates belong to the coherent- Ω and semi-coherent- θ' [15,16,32]. In the NA-20d specimen, no plate-type Ω/θ' precipitates were witnessed within the Al-matrix and even the grain boundaries were much free from precipitates (Fig. 7a-b). However, some of the irregular or spherical shaped Cu rich phases, possibly of θ -Al₂Cu were located inside the matrix and near nano-TiB₂ particles.

3.5. Tensile behaviour

The mechanical behaviour of NA-20d and AA-4 h specimens under tensile loading is presented in terms of engineering stress-strain curves in Fig. 9. The tensile behaviour of the as-built (AB) state was also considered for a comparison. The curve characteristics such as yield strength (σ_y), ultimate tensile strength (σ_{UTS}) and elongation to fracture (ϵ_f %) are summarised in Table 2. It is to note that NA-20d specimens displayed an excellent elongation to fracture with respect to both AA-4 h and AB states. Interestingly, NA-20d specimens also have an σ_{UTS} comparable to the AA-4 h ($\Delta\sigma_{UTS} \approx 29$ MPa). However, the σ_y of NA-20d specimens was much lower (≈ 276 MPa) than the AA-4 h (≈ 464 MPa) but comparable to the AB ($\Delta\sigma_y \approx 28$ MPa). The σ_y , σ_{UTS} and ϵ_f % of the AB state are 304 MPa, 378 MPa and 12.5%, respectively. The tensile curve of AB specimen exhibited the typical features of an LPBF A205 alloy: (i) upper yield point, (ii) a lower yield (iii) lüders band formation and (iv) Portevin-Le Chatelier (PLC) effect of type-C [15,37]. However, no PLC effect was observed in both NA and AA-4 h specimens.

Similar tensile properties were also reported elsewhere for the AB and conventional artificially aged (T7) LPBF-A205 alloy [32,37,39].

With respect to the casted-A205 (T7), the yield strength is similar but the ductility of the LPBF processed is always higher, see Table 2.

3.6. Fractography

The fractured analyses of NA-20d and AA-4h specimens by SEM are shown in Fig. 10. Both NA-20d and AA-4h specimens displayed a mix of fine and medium sized circular dimples representing the behaviour of a ductile fracture (Fig. 10a and b). Their corresponding SEM-BSE micrographs (Fig. 10c and d) disclosed the locations of the TiB₂ particles (violet arrows). They were seated inside the dimples of NA-20d and AA-4h specimens. However, in the AA-4h specimen, more θ -Al₂Cu particles (red arrows) were observed. Owing to the finer size of the TiB₂ and θ -Al₂Cu particles, they were distinguished by performing EDS spot analysis, see supplementary file (Fig S3).

The cross-sectional micrographs perpendicular to the fractured surface were also analysed (Fig. 10e and f). They revealed the presence of micro-voids at the TiB₂ particles/agglomerates (violet arrow) in the NA-20d and AA-4h specimen. Besides these, in the AA-4h specimen, there were multiple cracks (high aspect ratio) detected, marked as yellow arrows (Fig. 10f).

4. Discussion

4.1. Age hardening behaviour

The LPBF-A205 alloy demonstrated a considerable amount of hardening during NA (Fig. 2). The increase in hardness from NA-0 days to NA-20 days was around 27 HV. The gradual increase in hardness has been attributed to the formation and growth of disordered Ag-Mg co-clusters [18,43–45]. Such a gradual increment in hardness was supported by the DSC spectra (Fig. 3a). The increase in the peak area of Ag-Mg co-clusters dissolution with NA time indicates that their volume fraction continued to increase. However, we did not observe further increment of hardness after 20 days (Fig. 2). This could be due to the growth of co-clusters above a critical size which does not have further influence on hardness [59]. The formation of other known clusters in an Al-Cu-Mg alloy such as Cu-Mg and Cu-Cu was not observed in NA samples (Fig. 3a). The peak dissolution temperature of Cu-Mg and Cu-Cu clusters occurred in the range of 200–230°C [59,60] and 140–190°C [61–63], respectively. These peaks were not detected by DSC in the present case. The absence of such clusters can be explained based on the

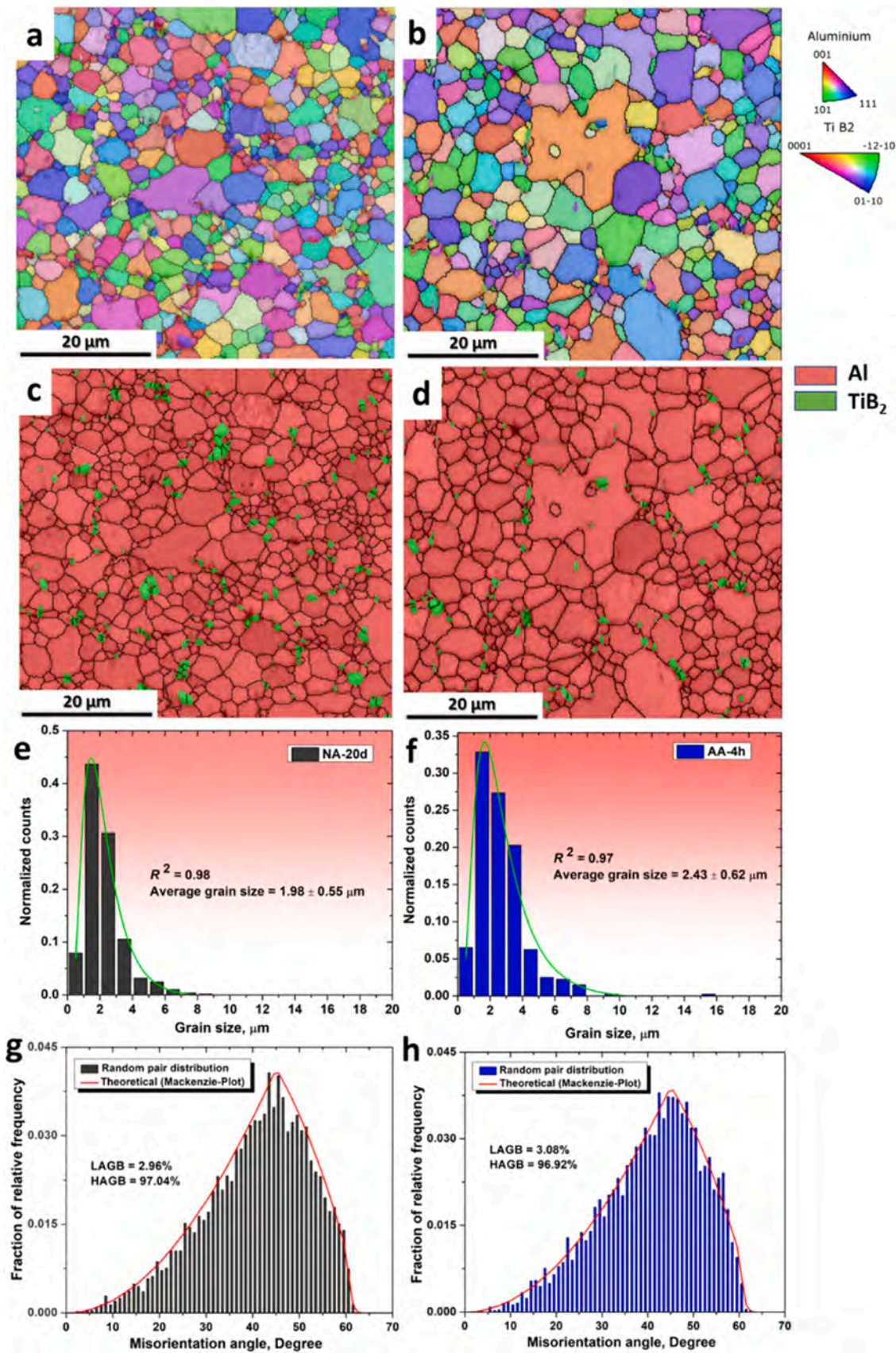


Fig. 5. EBSD micrographs of A205 samples post-processed with NA-20d (a, c and e) and AA-4 h (b, d and f). Showing (a and b) IPF map, (c and d) phase map, (e and f) grain size distribution and (g and h) distribution of misorientation angles.

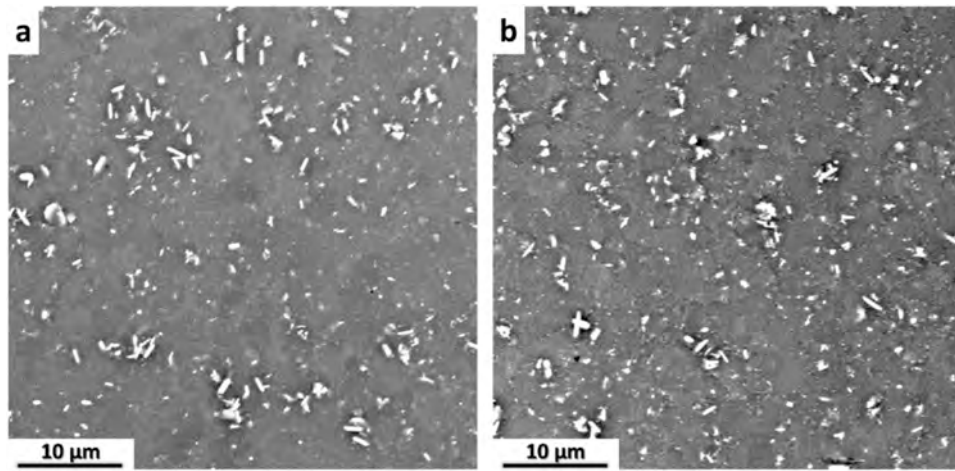


Fig. 6. SEM-BSE micrographs of (a) NA-20d and (b) AA-4h specimen.

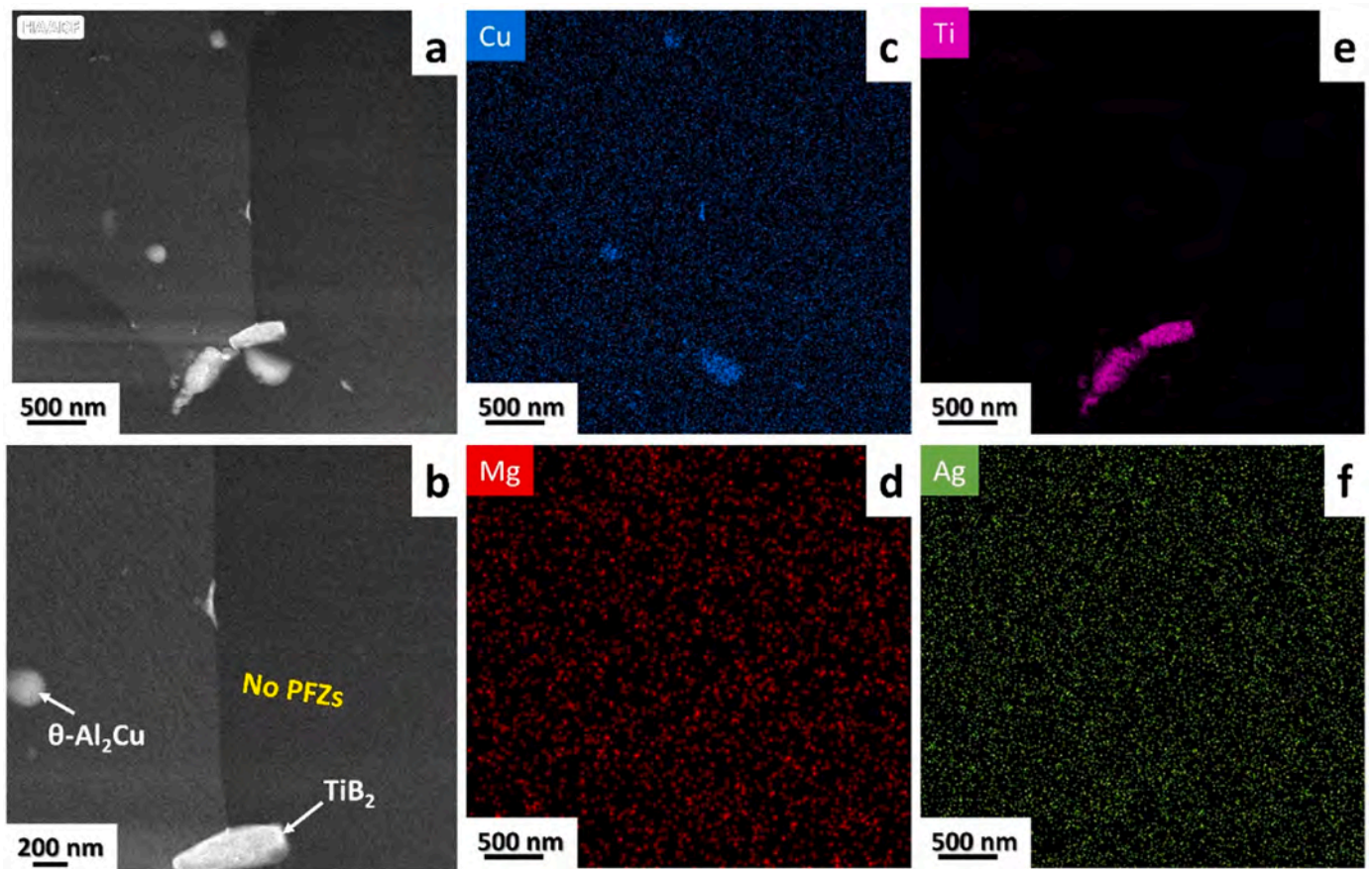


Fig. 7. NA-20d (a-b) HAADF-STEM micrographs and (c-f) EDS maps of the (a) region.

results of Nagai et al. [19] and Ferragut et al. [20], who have studied the role of Ag on early cluster formation in an Al-Cu-Mg alloy. They observed that, a minor addition of Ag stabilizes the Mg-vacancy clusters during quenching or in the initial stages of aging by forming Ag-Mg-vacancy complexes. This was due to the stronger binding energy of Mg and Ag atoms with the vacancies than with the Cu atoms [43,44].

Unlike the NA condition, the hardening response of AA at 190°C was quite steep (Fig. 2). Just after 2 h of aging there was a sudden increase in hardness to around 138 HV and it reached its peak value after 4 h (144 HV). The sudden rise of strength has been associated with the precipitation of plate-type coherent Ω -Al₂Cu and semi-coherent θ' -Al₂Cu phase,

see Fig. 8b. Both Ω and θ' are considered as main strengthening phases and can precipitate simultaneously through independent mechanisms [15,32]. Ω forms from the Ag-Mg co-clusters on {111} Al planes whereas θ' prefers to nucleate at the dislocations on {100} by the diffusion of Cu atoms during early stages of artificial aging [25]. After reaching the peak hardness, the AA specimen maintained the hardness up to 8 h, this could be due to the stability of the microstructure. Both Ω and θ' plates possess good thermal stability [29]. Additionally, Ω offers excellent coarsening resistance in the range of 150–200°C [28,31]. Hutchinson et al. reported that Ω plates kept their thickness below 6 nm even after 1000 h of exposure at 200°C [28]. Aging at 190°C for more than 8 h caused a slight

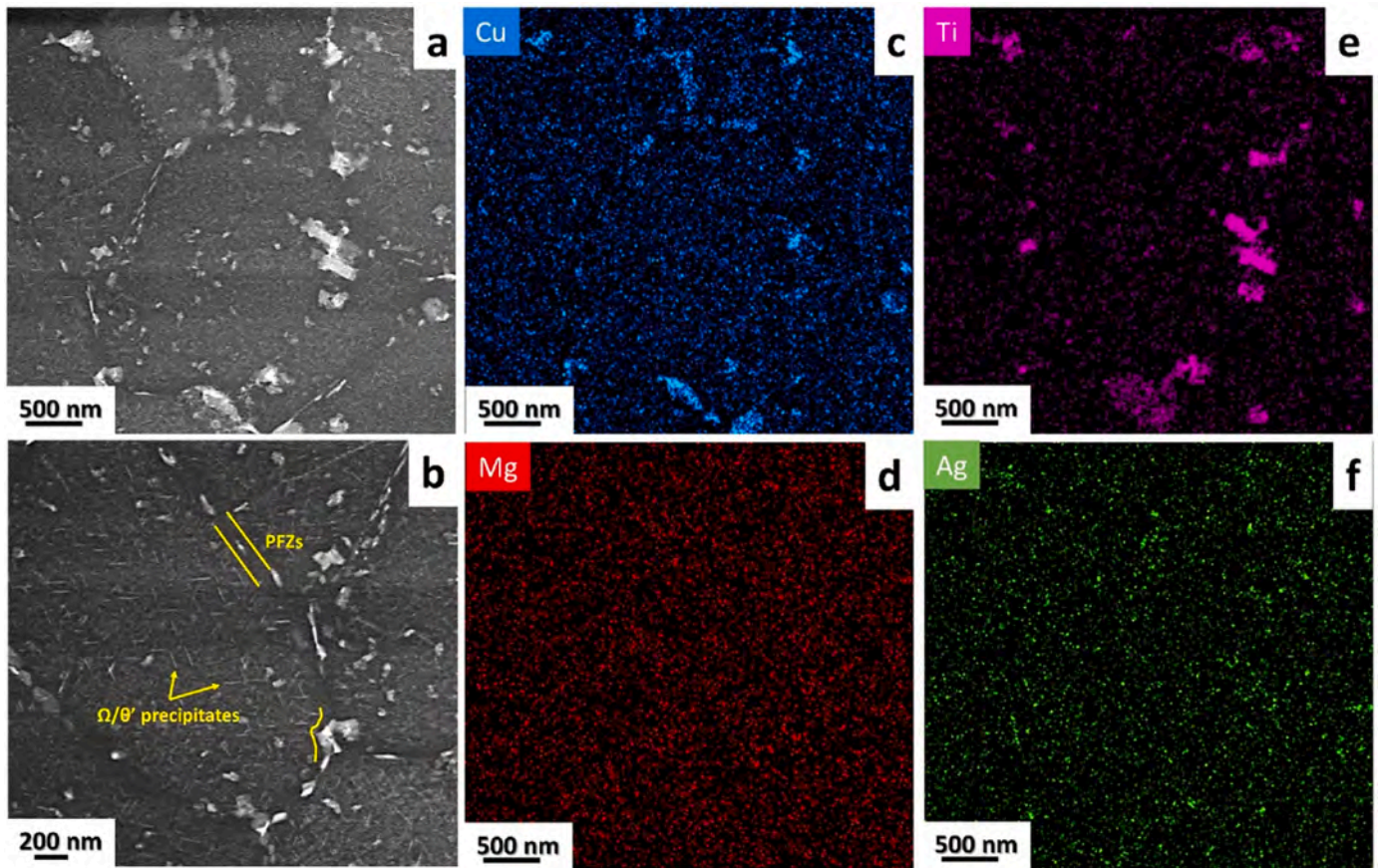


Fig. 8. AA-4h (a-b) HAADF-STEM micrographs and (c-f) EDS maps of the (a) region.

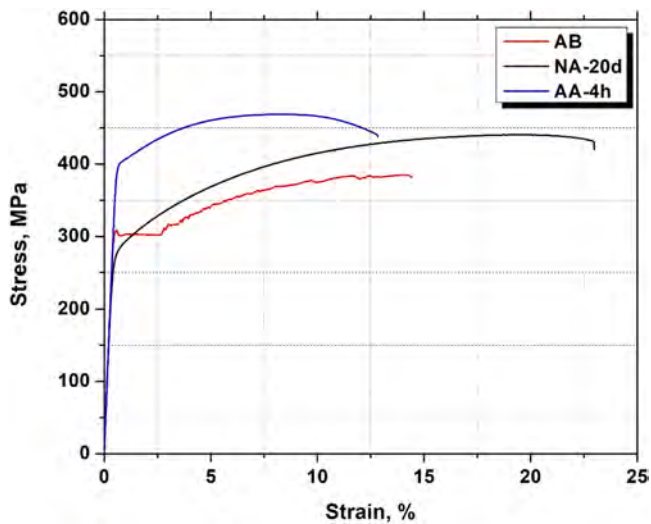


Fig. 9. Engineering stress-strain curves of LPBF-A205 alloy for various conditions.

decrease in the hardness. This might be due to the coarsening of the pre-precipitated equilibrium θ - Al_2Cu phase near the TiB_2 particles/at the grain boundaries along with the growth of θ' precipitates within the grains [30].

4.2. Strengthening mechanisms

The tensile behaviour (Fig. 9) indicates that the properties of the

Table 2

Characteristics of tensile curves for various conditions.

Condition	Micro-hardness, HV	σ_y , MPa	σ_{UTS} , MPa	ϵ_f , %
NA-20d (T4)	137 ± 2	276.2 ± 3.0	434.6 ± 4.4	20.4 ± 1.9
AA-4h (T6)	144 ± 6	397.2 ± 3.6	463.7 ± 5.2	11.6 ± 1.1
AB	113 ± 4	304.0 ± 3.0	378.0 ± 6.0	12.5 ± 1.6
Cast A205 (T7)	-	441 ± 1.4	501 ± 6.7	5.3 ± 1.6
LPBF A205 (T7)	≈ 152	370 ± 9	435 ± 13	7.3 ± 0.3

A205 alloy are strongly influenced by the post processing heat treatment. NA-20d demonstrated excellent ductility whereas AA-4h possessed highest strength. The difference in such behaviour has been attributed to their different microstructural features such as Ag-Mg co-clusters, Ω/θ' precipitates, solid solution (SS) and grain (GB) or cell boundaries. Pre-existence of TiB_2 particles in the A205 powders further strengthens the material [15,16,30]. These microstructural features contribute to the increment in the yield strength by various strengthening mechanisms. The estimation of the total yield strength in AB, NA-20d and AA-4h conditions can be obtained by the sum of their individual strengthening increments [15]:

$$\sigma_{\text{Total}} = \Delta\sigma_{\text{TiB}_2} + \Delta\sigma_{\text{Ag-Mg co-cluster}} + \Delta\sigma_{\Omega/\theta' \text{ precipitates}} + \Delta\sigma_{\text{GB}} + \Delta\sigma_{\text{SS}} + \sigma_0 \quad (4)$$

Where σ_0 is the lattice friction in pure Al (20 MPa) [15]. The contributions from all the strengthening mechanisms in various conditions and the constants utilized for calculations are presented in Table 3 and

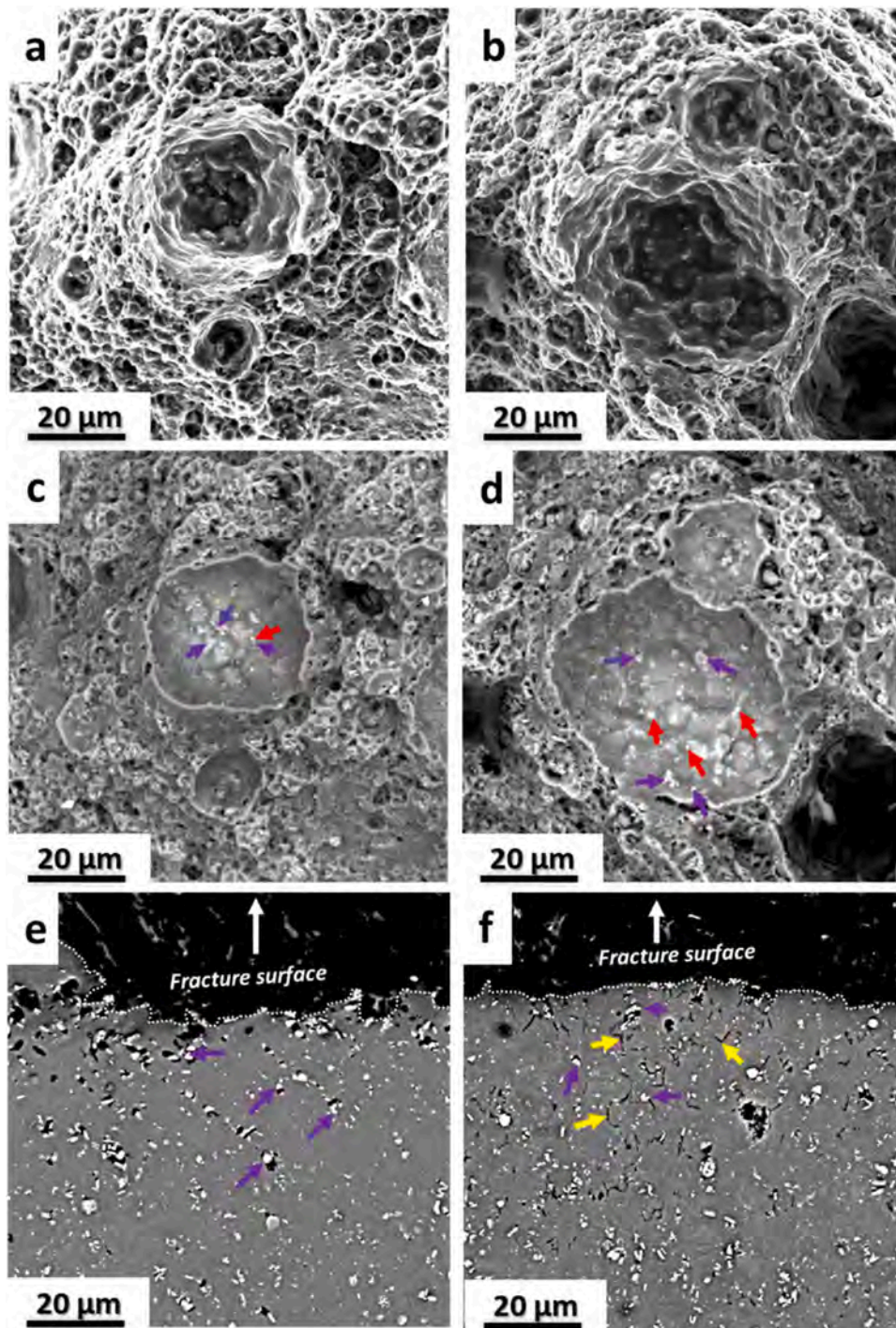


Fig. 10. SEM micrographs of the fractured surface of NA-20d (a, c, and e) and AA-4 h (b, d, and f); SE images (a and b); and their corresponding BSE images (c and d); BSE images of cross-sections perpendicular to the fractured surface (e and f). (violet, red and yellow arrow showing TiB_2 particles, $\theta\text{-Al}_2\text{Cu}$ and cracks, respectively).

Table 4, respectively.

4.2.1. Strengthening from TiB_2 particles

The presence of a ceramic component in the matrix improves the yield strength of the material by multiple strengthening mechanism: (i) load-bearing strengthening, (ii) Orowan strengthening, (iii) modulus mismatch strengthening, and (iv) coefficient of thermal expansion (CTE) mismatch strengthening.

The volume fraction (V_p), average diameter (d_p) and inter-particle distance between the TiB_2 particles (λ) were obtained from the SEM-BSE micrographs, as we take the advantage of atomic contrast to

distinguish different phases. The process followed in the estimation of these parameters is presented in Fig S2 of a supplementary file. Being the same material (A205), V_p , d_p and λ are considered the same for all the conditions namely AB, NA-20d and AA-4 h.

4.2.1.1. Load-bearing strengthening. The presence of TiB_2 particles enhances the strength of the material by directly transferring the load from the matrix to them [15,16]. The load-bearing strengthening contribution to the yield strength can be expressed as [14].

Table 3

Summary of the strengthening factors in various conditions.

Strengthening factors	AB, MPa	NA-20d, MPa	AA-4 h, MPa
σ_0	20	20	20
$\Delta\sigma_{GB}$	165.90	99.49	89.81
$\Delta\sigma_{SS}$	24.78	66.24	-
$\Delta\sigma_{TiB_2}$	40.31	37.41	37.41
$\Delta\sigma_{Ag-Mg \text{ co-cluster}}$	44.05	66.12	-
$\Delta\sigma_{\Omega/\theta \text{ precipitates}}$	-	-	254.90
σ_{Total}	295.04	289.26	402.12
σ_y	304.00	276.20	397.20
$\sigma_y - \sigma_{Total}$	8.96	-13.06	-4.92

Table 4

Summarizing different parameters with their physical meaning utilized in various strengthening mechanism [15,16,59,64,70,71].

Strengthening mechanism	Parameter	Value	Physical meaning
Al	G_m	26.9 GPa	Shear modulus
	M	3.06	Taylor factor for polycrystalline
	b	0.286 nm	Burger vector
	Γ	1.1×10^{-15} MPam ²	Dislocation line tension
	σ_0	20 MPa	Resistance to glide dislocation in the lattice
$\Delta\sigma_{GB}$	k	0.14 and 0.17 MPa \sqrt{m}	Obstacle to dislocation by grain boundary
$\Delta\sigma_{CTE}$	β_{CTE}	1.25	Geometric constant
$\Delta\sigma_{Modulus-TiB_2}$	α_{mt}	0.5	Dislocation strengthening coefficient
$\Delta\sigma_{Modulus-Clusters}$	α_{mc}	0.096	Constants from dislocation-precipitate interaction
	β_{mc}	0.76	Constant for FCC metal
$\Delta\sigma_{CS-Clusters}$	α_c	2.6 GPa	Constant for FCC metal
$\Delta\sigma_{\Omega/\theta \text{ precipitates}}$	γ_i	0.14	Specific interfacial energy between precipitate and matrix phase

$$\Delta\sigma_{LB} = V_p \frac{1}{2} \sigma_m \quad (5)$$

Where V_p is the volume fraction of TiB_2 particles and σ_m is the yield strength of the matrix ($\sigma_m = 289$ MPa) [15]. The V_p was found to be around 1.3%. The increment in σ_y by the load-bearing strengthening was calculated to be 1.89 MPa.

4.2.1.2. Orowan strengthening. During deformation, the hard TiB_2 particles cannot be cut-off by dislocations but instead they are by-passed by forming dislocation loops. This dislocation looping decreases the dislocations mean free path and the material experiences strengthening. The increase in yield strength by Orowan strengthening can be calculated as [15,16].

$$\Delta\sigma_{Orowan} = \frac{0.13 G_m b}{\lambda} \ln \frac{d_p}{2b} \quad (6)$$

Where G_m is the shear modulus of the matrix (26.9 GPa), b is the burger vector (0.286 nm), d_p is the average particle diameter and λ is the inter-particle distance between the particles. The d_p and λ were calculated from SEM-BSE images and resulted as 0.72 μm and 3.26 μm , respectively. The Orowan strengthening was about 2.20 MPa.

4.2.1.3. Modulus mismatch strengthening. An increment in the yield strength can be also due to the elastic modulus mismatch between the matrix and the particles [16]. It can be calculated as:

$$\Delta\sigma_{Modulus-TiB_2} = \sqrt{3} \alpha_{mt} G_m b \sqrt{\rho_{Modulus}} \quad (7)$$

$$\rho_{Modulus} = \frac{6 V_p \epsilon_y}{b d_p} \quad (8)$$

Where α_{mt} is a constant with a value of 0.5, it represents dislocation strengthening coefficient [16], $\rho_{Modulus}$ is the dislocation density arising due to the modulus mismatch, and ϵ_y is the yield strain of the composite. The contribution of modulus hardening to the yield strength resulted as 9.44 MPa.

4.2.1.4. Coefficient of thermal expansion (CTE) mismatch strengthening. Additional dislocations are generated at the interface of Al-matrix and TiB_2 particles due to the difference in their coefficient of thermal expansion (CTE) and are responsible for the increment in strength of the material. The CTE of Al-matrix is $23.5 \times 10^{-6} K^{-1}$ and for TiB_2 is $7.8 \times 10^{-6} K^{-1}$ [16], thus the $\Delta CTE_{Al-TiB_2} = 16.8 \times 10^{-6} K^{-1}$. During processing or post processing steps involving temperature changes such as solidification in the case of AB or solution-quenching for NA-20d and AA-4 h state, the estimation of a dislocation density and an increment of the strength can be calculated from the following equations [15,16]:

$$\Delta\sigma_{CTE} = \beta_{CTE} G_m b \sqrt{\rho_{CTE}} \quad (9)$$

$$\rho_{CTE} = \frac{12 \Delta CTE \Delta T V_p}{b d_p (1 - V_p)} \quad (10)$$

Where β_{CTE} is a geometric constant of 1.25 [15], ρ_{CTE} is dislocation density arising due to CTE mismatch, ΔCTE is the thermal expansion coefficient difference between matrix and ceramic component and ΔT is the temperature difference. The value of ΔT is 635 K for the AB state i.e., from melting to room temperature and 505 K for NA-20d and AA-4 h i.e., from solutioning temperature to room temperature. The dislocation generation and/or annihilation during artificial aging was neglected. The increment in the yield strength arising from the ΔCTE mismatch is around 26.78 MPa for AB state and 23.88 MPa for NA-20d and AA-4 h conditions.

4.2.2. Strengthening from Ag-Mg co-clusters

The presence of disordered clusters in the matrix increases the strength by two mechanisms: (i) modulus mismatch strengthening and (ii) coherent strengthening. The former is due to the difference in the elastic modulus between the matrix and atomic clusters or co-clusters, whereas the latter is due to the lattice mismatch. The strengthening contributions to the yield strength can be obtained from the following equation [15,59]:

$$\Delta\sigma_{Modulus-Clusters} = 1.4 \alpha_{mc}^{3/2} \Delta G^{3/2} f^{1/2} b \left(\frac{\Gamma}{b} \right)^{\frac{3\beta_{mc}}{2}-1} (2\pi\Gamma)^{-1/2} \quad (11)$$

$$\Delta\sigma_{CS-Clusters} = M \alpha_c (G_m \epsilon_c)^{3/2} \left(\frac{rf}{0.5 G_m b} \right)^{1/2} \quad (12)$$

Where α_{mc} and β_{mc} are constants that can be obtained from a dislocation-precipitate interaction model, their values are 0.096 and 0.76 respectively [59]. ΔG is the difference in the shear modulus of Al-matrix and Ag-Mg co-clusters ($\Delta G = 2.6$ GPa) [15]. Γ is the line tension of a dislocation in the matrix which is usually approximated as $\frac{1}{2} G_m b^2$ [59]. α_c is a constant of 2.6 for FCC metals [64] and ϵ_c is the strain associated with the atomic cluster misfit with the matrix, which is around 1% for Ag-Mg co-clusters in the A205 alloy [15]. f and r are the volume fraction and average radius of the clusters. The volume fraction of Ag-Mg co-clusters in NA-20d has been approximated based on the Ag and Mg concentration inside the grains by EDS spot analysis and with an assumption that Ag and Mg form clusters in 1:1 at. ratio. This assumption was based on multiple atom probe tomography (APT) studies on Al-Cu-Mg-Ag alloy [21,25,26]. The concentration of Mg was ≈ 0.25 wt% which corresponds to the volume fraction (f) of clusters as 0.0071. It has been

reported that, Ag-Mg co-clusters were hard to be identified by TEM, this seems true also in the present investigation, see Fig. 7a, and a more advanced techniques such as APT has been suggested [22,65]. However, in the present study, the average radius of the co-clusters in NA-20d was assumed as 1.8 nm (≈ 50 atoms). It was an average of the Ag-Mg co-cluster size (10–100 atoms) observed in the early stages of aging by various APT studies [47,66]. f in the AB state was taken as 0.0034 from the similar study on LPBF of A205 alloy with the same linear energy density (0.24 J/mm) [15]. In the AA-4 h specimen, as the DSC did not show any sign of Ag-Mg co-clustering i.e., no endothermic peak in Fig. 3a, it is reasonable to neglect the hardening from atomic clusters. The strengthening contribution obtained from $\Delta\sigma_{\text{Modulus-Clusters}}$ in AB and NA-20d state were 1.41 MPa and 2.07 MPa, respectively and from $\Delta\sigma_{\text{CS}}$ in AB and NA-20d state are 42.64 MPa and 64.05 MPa respectively.

4.2.3. Contribution from plate-type Ω/θ' precipitates

Interaction of dislocations with the precipitates can strengthen the material by either dislocation looping (Orowan strengthening) or by dislocation shearing (interfacial strengthening) mechanisms [34,36]. The character of a dislocation-precipitate interaction mechanism depends on its crystal structure, aspect ratio, volume fraction and number density.

There have been number of studies demonstrating that Ω plates were sheared by dislocations [35,67]. In contrast, θ' precipitates interacts by forming dislocation loops [68,69]. However, being precipitated on $\{111\}$ Al plane, Ω plates provides more effective strengthening than $\{100\}$ θ' plates [35,36]. For simplicity, it was assumed that all the plate-type precipitates (Ω and θ') in an AA-4 h condition strengthen the material by dislocation shearing. No strengthening contribution from precipitates in NA-20d and AB conditions were considered, as these needle-type matrix precipitates were not observed in the NA-20d condition (Fig. 7), nor such precipitates have been reported in the AB state elsewhere [16]. Nei and Muddle [34] have developed a model on dislocation shearing of plate-type precipitates that nucleated on $\{111\}$ plane of Al, considering the effect of precipitate shape, orientation, and distribution on the increment in the yield strength of the alloy:

$$\Delta\sigma_{\Omega/\theta' \text{ precipitates}} = \frac{1.211M\bar{d}_i\gamma_i^{3/2}}{t_i^2} \sqrt{\frac{bf_v}{\Gamma}} \quad (13)$$

Where $M=3.06$ is the Taylor factor for polycrystalline materials, Γ is dislocation line tension, γ_i is the interfacial energy corresponding to the new interface (0.14 J/m²) [36], f_v is the volume fraction of Ω precipitates, calculated from the TEM micrographs as 0.019 (Eqs. 1–3). t_i and d_i are average plate thickness and diameter with a value of 1.7 nm and 54 nm, respectively. The strengthening increment to the yield strength by the Ω/θ' precipitates was 254.90 MPa.

4.2.4. Grain boundary strengthening

The strengthening contribution from the GBs can be calculated with the classical Hall-Petch relation [70].

$$\Delta\sigma_{\text{GB}} = kd^{-1/2} \quad (14)$$

Where k is the Hall-Petch coefficient, which represents the ability of the GBs to impede the dislocation motion. The value of k ranges from 0.04 MPa $\sqrt{\text{m}}$ for a fully recrystallized grain to 0.26 MPa $\sqrt{\text{m}}$ for a highly deformed ultra fine grain [70,71]. In the present study, two distinctive values of k have been considered: 0.17 MPa $\sqrt{\text{m}}$ for representing cellular microstructure of the AB state, the θ -Al₂Cu cell boundaries offers high obstacle to dislocation motion [15] and 0.14 MPa $\sqrt{\text{m}}$ representing matrix with a large number of high-angle grain boundaries (HAGB) [70] for the case of NA-20d and AA-4 h state (Fig. 5g and Fig. 5h). d is the average grain size of the alloy as 0.91 μm [30], 1.98 μm and 2.43 μm for AB, NA-20d and AA-4 h conditions (Fig. 5e-f). The strength increments by grain boundary strengthening in an AB, NA-20d and AA-4 h state are

165.90 MPa, 99.49 MPa and 89.81 MPa, respectively. Such a considerable strengthening increment to the yield strength was due to their finer grain sizes which is a typical characteristic of a LPBF process.

4.2.5. Solid solution strengthening

The strengthening increment by solid solution can be calculated by the following equation [23].

$$\Delta\sigma_{\text{SS}} = \sum_{i=\text{element}} k_i \times c_{\text{ss},i}^n \quad (15)$$

Where k_i is the strengthening contribution related to the solute-dislocation interaction. For Cu and Mg, the $k_{\text{Cu}} = 13.8$ MPa/wt% and $k_{\text{Mg}} = 18.6$ MPa/wt%, respectively [15,23]. It was reported that Ag atoms have no strengthening effect in Al alloys due to their negligible lattice misfit [72]. $c_{\text{ss},i}^n$ is the concentration of solute i in the solid solution and n is a constant with a value of 1 [23]. The solid solution strengthening in the AA-4 h state can be neglected, since Cu, Mg and Ag were all responsible for the precipitation of Ω , θ and θ' (Al₂Cu) and were either consumed by the precipitates during the process of nucleation and growth or constrained within the Al-precipitate interfaces [23,25,26]. In the NA-20d state, only solid solution strengthening from Cu atoms was considered, as it was assumed that all the Mg atoms bind to the Ag atoms to form Ag-Mg co-clusters. The concentration of Cu was around 4.8 wt%. In the AB state, both Cu and Mg atoms contribute to the strengthening. The concentration of Cu and Mg were taken from the work of Jiang et al. [15], which have reported the solute concentration of A205 alloy in AB state processed by LPBF. The Cu and Mg concentration are 1.58 wt% and 0.16 wt%, respectively. The solid solution strengthening ($\Delta\sigma_{\text{SS}}$) in the AB and NA-20d state were 24.78 MPa and 66.24 MPa, respectively.

A summary of all the contributions from various strengthening factors in the AB, NA-20d and AA-4 h states are presented in the Table 3. Strengthening due to the presence of TiB₂ particles was around ≈ 40 MPa in the AB and ≈ 37 MPa for both NA-20d and AA-4 h conditions. Being processed by LPBF, the grain size strengthening significantly contributes to all the conditions. Although the AB state has a cellular microstructure (eutectic θ -Al₂Cu cell boundaries) which offers much higher resistance to the dislocation motion than in NA-20d and AA-4 h states (≈ 165 MPa). Strengthening in a NA-20d state was majorly due to coherent strengthening from disordered Ag-Mg co-clusters (≈ 64 MPa) and solid solution strengthening by Cu solutes (≈ 66 MPa), whereas in the AA-4 h state, interfacial strengthening was dominated by the presence of high number density of plate-type Ω/θ' precipitates (≈ 254 MPa). The calculated yield strength in various processed and post-processed conditions were within the 5% deviations of the experimental values (Table 3) indicating a good match with the experimental.

Post to the yield strength, both NA-20d and AA-4 h conditions neither displayed the Lüders band formation nor the serrated flow behaviour (PLC effect), see Fig. 9. This has been associated with the lack of free Mg atoms in the matrix. In the AB state, during plastic deformation, repeated locking and unlocking of mobile dislocations with free Mg atoms in the matrix was responsible for such behaviour [37,39]. In the NA-20d state, Mg binds very strongly to the Ag and readily forms Ag-Mg co-clusters [19,20]. In the AA-4 h state, Mg atoms are being consumed in the process of precipitation and stabilization of Ω plates [24,25,31]. It is widely known that Mg and Ag tends to segregate at the broad interface of Ω -plates/ α -Al during artificial aging [24]. As Mg and Ag segregation helps to reduces the misfit strain energy arising due to growth of coherent- Ω plates [24,28].

4.3. Failure mechanism

During tensile deformation, after necking, the material deforms in an inhomogeneous way due to stress gradient along the gauge-section. This inhomogeneous deformation is associated with the formation of microstructural defects [39]. Because of this reason, assessing the

microstructure along the length of gauge section helps to understand the initiation of failure.

NA-20d specimens demonstrated excellent ductility with respect to the AA-4 h specimens, thus by observing the tensile specimens perpendicular to the fractured surface, it was beneficial to gain insights into the possible failure mechanisms. In the NA-20d, micro-voids were formed near individual TiB₂ particles and near their agglomerations (Fig. 10e (violet arrow)). The same was also observed by fractography under BSE mode that showed TiB₂ particles sitting inside the dimples (Fig. 10c). However, in the AA-4 h specimen, besides observing these micro-voids near TiB₂ particles, there were multiple cracks present (Fig. 10f (yellow arrow)). These cracks were likely to be located at the grain boundaries. During deformation, the matrix precipitates (Ω and θ') were either being sheared or by-passed by dislocations. At high strain values, the matrix becomes hardened, and dislocations are piled-up at the grain boundaries causing a highly localized strain. This results in a nucleation of voids near precipitate free zone (PFZs) and then growth along these regions causing an intergranular fracture [73,74]. No such grain boundary cracks were observed in the NA-20d specimen (Fig. 10e) as there were neither grain boundary precipitates which promotes weak PFZs nor high strength Ω/θ' -Al₂Cu precipitates which hardens the Al-matrix relative to grain boundaries (Fig. 7a-b). Thus, in NA-20d, the failure initiation is solely at TiB₂ particles which were located at the grain boundaries and grain triple junctions (Fig. 7b), that also leads to intergranular fracture at higher strains.

5. Conclusions

In the present study, we have demonstrated the response of A205 alloy processed by LPBF towards natural aging (NA) i.e., solution treatment followed by aging at room temperature, and compared it with an artificial aging (AA). The following conclusions can be drawn:

1. The NA of an A205 alloy achieved its peak hardness in around 20 days at a temperature of $\approx 28^\circ\text{C}$, whereas it took 4 h at 190°C in the case of AA. The difference between their peak hardness was ≈ 10 HV.
2. The tensile behaviour of NA-20d and AA-4 h i.e., their peak aged conditions, were compared. The ultimate tensile strength of NA-20d was comparable to AA-4 h, with a difference of only 6.2%, and a considerable improvement in the elongation to fracture of around 43% than AA-4 h. The yield strength however was 30% lower than AA-4 h.
3. The major strengthening contributions for the NA-20d were coherency strengthening by the Ag-Mg co-clusters and solid solution strengthening by Cu atoms, whereas strengthening by the dislocation shearing of Ω/θ' plate-type precipitates were dominant in AA-4 h.
4. Grain boundary strengthening also contributed significantly to both NA-20d and AA-4 h, because of their fine grains, 1.98 μm and 2.43 μm respectively.
5. Fractography studies revealed different failure mechanism in NA-20d and AA-4 h. In NA-20d, the failure initiates solely by the formation of micro-voids at the individual TiB₂ particles and at their agglomerates, whereas in the AA-4 h, it was both by micro-void formation at TiB₂ particles and cracking along grain boundaries due to formation of PFZs.

Both post-processing heat treatments improved the mechanical property of the A205 alloy with respect to as-built state. The NA-20d gives good-strength and high-ductility whereas, the AA-4h provides high-strength and good-ductility combination to the alloy with respect to its different processing and post-processing conditions, thus, one can get benefitted from both the heat treatments based on their intended application.

CRedit authorship contribution statement

Paolo Fino: Supervision, Project administration, Funding acquisition. **Mariangela Lombardi:** Supervision, Project administration, Funding acquisition. **Jayant Barode:** Writing – original draft, Investigation, Conceptualization. **Ashok Vayyala:** Investigation, Formal analysis. **Alberta Aversa:** Writing – review & editing, Supervision, Methodology, Conceptualization. **Luyan Yang:** Methodology, Investigation. **Joachim Mayer:** Supervision.

Declaration of Competing Interest

The authors declare that they have no known competing financial interests or personal relationships that could have appeared to influence the work reported in this paper.

Data availability

Data will be made available on request.

Acknowledgements

The study was carried out within the MOST – Sustainable Mobility National Research Center and received funding from the European Union Next-GenerationEU (Piano nazionale di ripresa e resilienza (PNRR) – missione 4 componente 2, investimento 1.4 – D.D. 1033 17/06/2022, CN00000023). This manuscript reflects only the authors' views and opinions, neither the European Union nor the European Commission can be considered responsible for them.

The authors would like to thank Mr. Dario Pezzini for carrying out the tensile test.

Appendix A. Supporting information

Supplementary data associated with this article can be found in the online version at [doi:10.1016/j.mtcomm.2024.108978](https://doi.org/10.1016/j.mtcomm.2024.108978).

References

- [1] I. Yadroitsev, I. Yadroitsava, A. Du Plessis, E. MacDonald, *Fundamentals of Laser Powder Bed Fusion Of Metals*, Elsevier, 2021.
- [2] P. Bajaj, A. Hariharan, A. Kini, P. Kürnsteiner, D. Raabe, E.A. Jägle, *Steels in additive manufacturing: a review of their microstructure and properties*, *Mater. Sci. Eng. A* 772 (2020) 138633.
- [3] L. Zhang, H. Attar, *Selective laser melting of titanium alloys and titanium matrix composites for biomedical applications: a review*, *Adv. Eng. Mater.* 18 (2016) 463–475.
- [4] N.T. Aboulkhair, M. Simonelli, L. Parry, I. Ashcroft, C. Tuck, R. Hague, *3D printing of Aluminium alloys: additive manufacturing of aluminium alloys using selective laser melting*, *Prog. Mater. Sci.* 106 (2019) 100578, <https://doi.org/10.1016/j.pmatsci.2019.100578>.
- [5] C.Y. Yap, H.K. Tan, Z. Du, C.K. Chua, Z. Dong, *Selective laser melting of nickel powder*, *Rapid Prototyp. J.* 23 (2017) 750–757, <https://doi.org/10.1108/RPJ-01-2016-0006>.
- [6] H.R. Kotadia, G. Gibbons, A. Das, P.D. Howes, *A review of Laser Powder Bed Fusion Additive Manufacturing of aluminium alloys: microstructure and properties*, *Addit. Manuf.* 46 (2021) 102155, <https://doi.org/10.1016/j.addma.2021.102155>.
- [7] S.A. Butler, *An aluminium-copper alloy*, UK Patent: GB2334966A, 2003.
- [8] AMS AM Additive Manufacturing Metals, *Aluminum Alloy Powder 4.6Cu - 3.4Ti - 1.4B - 0.75Ag - 0.27Mg*, SAE International, 2021. <https://doi.org/10.4271/AMS7033>.
- [9] A. Aversa, G. Marchese, A. Saboori, E. Bassini, D. Manfredi, S. Biamino, D. Ugues, P. Fino, M. Lombardi, *New aluminum alloys specifically designed for laser powder bed fusion: a review*, *Materials* 12 (2019) 1007, <https://doi.org/10.3390/ma12071007>.
- [10] M. Chen, X. Li, G. Ji, Y. Wu, Z. Chen, W. Baekelant, *Novel composite powders with uniform TiB₂ nano-particle distribution for 3D printing*, *Appl. Sci.* 7 (2017), <https://doi.org/10.3390/app7030250>.
- [11] X.P. Li, G. Ji, Z. Chen, A. Addad, Y. Wu, H.W. Wang, J. Vleugels, J. Van Humbeeck, J.P. Kruth, *Selective laser melting of nano-TiB₂ decorated AlSi10Mg alloy with high fracture strength and ductility*, *Acta Mater.* 129 (2017) 183–193, <https://doi.org/10.1016/j.actamat.2017.02.062>.
- [12] S. Tang, R. Ummethala, C. Suryanarayana, J. Eckert, K.G. Prashanth, Z. Wang, *Additive manufacturing of aluminum-based metal matrix composites — a review*,

- Adv. Eng. Mater. 2100053 (2021) 1–17, <https://doi.org/10.1002/adem.202100053>.
- [13] J.H. Martin, B.D. Yahata, J.M. Hundley, J.A. Mayer, T.A. Schaedler, T.M. Pollock, 3D printing of high-strength aluminum alloys, *Nature* 549 (2017) 365–369, <https://doi.org/10.1038/nature23894>.
- [14] C.S. Kim, I. Sohn, M. Nezafati, J.B. Ferguson, B.F. Schultz, Z. Bajestani-Gohari, P. K. Rohatgi, K. Cho, Prediction models for the yield strength of particle-reinforced unimodal pure magnesium (Mg) metal matrix nanocomposites (MMNCs), *J. Mater. Sci.* 48 (2013) 4191–4204, <https://doi.org/10.1007/s10853-013-7232-x>.
- [15] F. Jiang, L. Tang, S. Li, H. Ye, M.M. Attallah, Z. Yang, Achieving strength-ductility balance in a laser powder bed fusion fabricated TiB₂/Al–Cu–Mg–Ag alloy, *J. Alloy. Compd.* 945 (2023) 169311, <https://doi.org/10.1016/j.jallcom.2023.169311>.
- [16] S.I. Shakil, A.S. Zoeram, H. Pirgazi, B. Shalchi-Amirkhiz, B. Poorganji, M. Mohammadi, M. Haghsheenas, Microstructural-micromechanical correlation in an Al–Cu–Mg–Ag–TiB₂ (A205) alloy: additively manufactured and cast, *Mater. Sci. Eng. A* 832 (2022) 142453, <https://doi.org/10.1016/j.msea.2021.142453>.
- [17] ECKART GmbH, A20X powder- Technical Information Sheet, (2020).
- [18] C.-L. Tai, M.-C. Chen, T.-F. Chung, Y.-L. Yang, S.-L. Lee, T.-C. Tsao, Z. Shi, J. Lin, T.-C. Su, H.-R. Chen, J.-R. Yang, The nano-structural characterization of Ω and S phases in Al–5.1Cu–1.0 Mg–(0.4Ag) AA2024 aluminum alloys, *Mater. Sci. Eng. A* (2023) 145361, <https://doi.org/10.1016/j.msea.2023.145361>.
- [19] Y. Nagai, T. Honma, Z. Tang, K. Hono, M. Hasegawa, Coincidence Doppler broadening study of the pre-precipitation stage of an Al–Cu–Mg–Ag alloy, *Philos. Mag. A* 82 (2002) 1559–1572, <https://doi.org/10.1080/01418610208240037>.
- [20] R. Ferragut, A. Dupasquier, C.E. Macchi, A. Somoza, R.N. Lumley, L.J. Polmear, Vacancy – solute interactions during multiple-step ageing of an Al – Cu – Mg – Ag alloy, *Scr. Mater.* 60 (2009) 13–16, <https://doi.org/10.1016/j.scriptamat.2008.09.011>.
- [21] T. Honma, S. Yanagita, K. Hono, Y. Nagai, M. Hasegawa, Coincidence doppler broadening and 3DAP study of the pre-precipitation stage of an Al–Li–Cu–Mg–Ag alloy, *Acta Mater.* 52 (2004) 1997–2003, <https://doi.org/10.1016/j.actamat.2003.12.043>.
- [22] S. Bai, Z. Liu, X. Zhou, P. Xia, S. Zeng, Mg-controlled formation of Mg – Ag co-clusters in initial aged Al – Cu – Mg – Ag alloys, *J. Alloy. Compd.* 602 (2014) 193–198, <https://doi.org/10.1016/j.jallcom.2014.03.008>.
- [23] S. Bai, X. Yi, Z. Liu, On the role of Ag additions on the initial solute hardening and competitive precipitation of Al–Cu–Mg alloys, *J. Alloy. Compd.* 945 (2023) 169339, <https://doi.org/10.1016/j.jallcom.2023.169339>.
- [24] L. Reich, M. Murayama, K. Hono, Evolution of Ω phase in an Al–Cu–Mg–Ag alloy—a three-dimensional atom probe study, *Acta Mater.* 46 (1998) 6053–6062, [https://doi.org/10.1016/S1359-6454\(98\)00280-8](https://doi.org/10.1016/S1359-6454(98)00280-8).
- [25] S.P. Ringer, K. Hono, L.J. Polmear, T. Sakurai, Nucleation of precipitates in aged AlCuMg (Ag) alloys with high Cu: Mg ratios, *Acta Mater.* 44 (1996) 1883–1898, [https://doi.org/10.1016/S1359-6454\(95\)00314-2](https://doi.org/10.1016/S1359-6454(95)00314-2).
- [26] M. Murayama, K. Hono, Three dimensional atom probe analysis of pre-precipitate clustering in an Al–Cu–Mg–Ag alloy, *Scr. Mater.* 38 (1998) 1315–1319, [https://doi.org/10.1016/S1359-6462\(98\)00027-X](https://doi.org/10.1016/S1359-6462(98)00027-X).
- [27] J. Wang, Z. Liu, S. Bai, J. Cao, J. Zhao, L. Luo, Microstructure evolution and mechanical properties of the electron-beam welded joints of cast Al – Cu – Mg – Ag alloy, *Mater. Sci. Eng. A* 801 (2021) 140363, <https://doi.org/10.1016/j.msea.2020.140363>.
- [28] C.R. Hutchinson, X. Fan, S.J. Pennycook, G.J. Shiflet, On the origin of the high coarsening resistance of Ω plates in Al–Cu–Mg–Ag alloys, *Acta Mater.* 49 (2001) 2827–2841, [https://doi.org/10.1016/S1359-6454\(01\)00155-0](https://doi.org/10.1016/S1359-6454(01)00155-0).
- [29] S.P. Ringer, W. Yeung, B.C. Muddle, L.J. Polmear, Precipitate stability in AlCuMgAg alloys aged at high temperatures, *Acta Metall.* 42 (1994) 1715–1725, [https://doi.org/10.1016/0956-7151\(94\)90381-6](https://doi.org/10.1016/0956-7151(94)90381-6).
- [30] J. Barode, A. Vayyala, E. Virgillito, A. Aversa, J. Mayer, P. Fino, Revisiting heat treatments for additive manufactured parts: a case study of A20X alloy, *Mater. Des.* 225 (2023) 111566, <https://doi.org/10.1016/j.matdes.2022.111566>.
- [31] X.Y. Liu, Q.L. Pan, L.Y. Zheng, Q.R. Fu, F. Gao, M.X. Li, Y.M. Bai, Effect of aging temper on the thermal stability of Al–Cu–Mg–Ag heat-resistant alloy, *Mater. Des.* 46 (2013) 360–365, <https://doi.org/10.1016/j.matdes.2012.10.039>.
- [32] M. Avateffazeli, P.E. Carrion, B. Shachi-Amirkhiz, H. Pirgazi, M. Mohammadi, N. Shamsaei, M. Haghsheenas, Correlation between tensile properties, microstructure, and processing routes of an Al–Cu–Mg–Ag–TiB₂ (A205) alloy: additive manufacturing and casting, *Mater. Sci. Eng. A* 841 (2022) 142989, <https://doi.org/10.1016/j.msea.2022.142989>.
- [33] A. Kulkarni, D. Srinivasan, S. Kumar, P. Kumar, Precipitate evolution and thermal stability of A205 fabricated using laser powder bed fusion, *J. Mater. Sci.* 58 (2023) 2310–2333, <https://doi.org/10.1007/s10853-023-08163-6>.
- [34] J.F. Nie, B.C. Muddle, Microstructural design of high-strength aluminum alloys, *J. Phase Equilibria* 19 (1998) 543–551, <https://doi.org/10.1361/104597198770341734>.
- [35] M.R. Gazizov, A.N. Belyakov, R. Holmestad, M.Y. Gazizova, V.S. Krasnikov, P. A. Bezborodova, R.O. Kaibyshev, The deformation behavior of the {111}Al plates in an Al–Cu–Mg–Ag alloy, *Acta Mater.* 243 (2023) 118534, <https://doi.org/10.1016/j.actamat.2022.118534>.
- [36] M. Gazizov, R. Kaibyshev, Precipitation structure and strengthening mechanisms in an Al–Cu–Mg–Ag alloy, *Mater. Sci. Eng. A* 702 (2017) 29–40, <https://doi.org/10.1016/j.msea.2017.06.110>.
- [37] P. Mair, L. Kaserer, J. Braun, N. Weinberger, I. Letofsky-Papst, G. Leichtfried, Microstructure and mechanical properties of a TiB₂-modified Al–Cu alloy processed by laser powder-bed fusion, *Mater. Sci. Eng. A* 799 (2021) 140209, <https://doi.org/10.1016/j.msea.2020.140209>.
- [38] P. Mair, J. Braun, L. Kaserer, L. March, D. Schimbäck, I. Letofsky-Papst, G. Leichtfried, Unique microstructure evolution of a novel Ti-modified Al–Cu alloy processed using laser powder bed fusion, *Mater. Today Commun.* 31 (2022), <https://doi.org/10.1016/j.mtcomm.2022.103353>.
- [39] M.H. Ghoncheh, M. Sanjari, A.S. Zoeram, E. Cyr, B.S. Amirkhiz, A. Lloyd, M. Haghsheenas, M. Mohammadi, On the microstructure and solidification behavior of new generation additively manufactured Al–Cu–Mg–Ag–Ti–B alloys, *Addit. Manuf.* 37 (2021) 101724, <https://doi.org/10.1016/j.addma.2020.101724>.
- [40] M. Avateffazeli, S.I. Shakil, A. Hadadzadeh, B. Shalchi-Amirkhiz, H. Pirgazi, M. Mohammadi, M. Haghsheenas, On microstructure and work hardening behavior of laser powder bed fused Al–Cu–Mg–Ag–TiB₂ and AlSi10Mg alloys, *Mater. Today Commun.* 35 (2023) 105804, <https://doi.org/10.1016/j.mtcomm.2023.105804>.
- [41] M. Ghasri-Khoushani, H. Karimialavijeh, M. Pröbstle, R. Batmaz, W. Muhammad, A. Chakraborty, T.D. Sabiston, J.P. Harvey, Martin, Processability and characterization of A20X aluminum alloy fabricated by laser powder bed fusion, *Mater. Today Commun.* 35 (2023), <https://doi.org/10.1016/j.mtcomm.2023.105555>.
- [42] F. Bellelli, R. Casati, F. Larini, M. Riccio, M. Vedani, Investigation on two Ti–B-reinforced Al alloys for Laser Powder Bed Fusion, *Mater. Sci. Eng. A* 808 (2021), <https://doi.org/10.1016/j.msea.2021.140944>.
- [43] N. Ünlü, B.M. Gable, G.J. Shiflet, E.A. Starke, The effect of cold work on the precipitation of omega and theta prime in a ternary Al–Cu–Mg Alloy, *Metall. Trans. A* 34 (2003) 24–27, <https://doi.org/10.1007/s11661-003-0177-y>.
- [44] Y. Weng, Z. Jia, L. Ding, Y. Pan, Y. Liu, Q. Liu, Effect of Ag and Cu additions on natural aging and precipitation hardening behavior in Al–Mg–Si alloys, *J. Alloy. Compd.* 695 (2017) 2444–2452, <https://doi.org/10.1016/j.jallcom.2016.11.140>.
- [45] Y. Te Chen, S.L. Lee, H.Y. Bor, J.C. Lin, Effect of natural aging and cold working on microstructures and mechanical properties of Al–4.6Cu–0.5Mg–0.5Ag alloy, *Metall. Mater. Trans. A* 44 (2013) 2831–2838, <https://doi.org/10.1007/s11661-013-1611-4>.
- [46] I. Zuiiko, R. Kaibyshev, Aging behavior of an Al–Cu–Mg alloy, *J. Alloy. Compd.* 759 (2018) 108–119, <https://doi.org/10.1016/j.jallcom.2018.05.053>.
- [47] S. Bai, Z. Liu, P. Ying, J. Wang, J. Li, Investigation of modulus hardening of various co-clusters in aged Al–Cu–Mg–Ag alloy by atom probe tomography, *Mater. Sci. Eng. A* 668 (2016) 234–242, <https://doi.org/10.1016/j.msea.2016.05.016>.
- [48] T. Wang, H. He, K. Liu, Y. Yan, Z. Deng, J. Liao, W. Li, Mechanisms related to the influence of natural aging on the precipitation behavior of the A357 aluminum alloy during artificial aging, *Vacuum* 217 (2023) 112581, <https://doi.org/10.1016/j.vacuum.2023.112581>.
- [49] Z. Deng, H. He, K. Liu, X. Tao, Z. Shang, Z. Gong, X. Wang, The influence of natural aging on the precipitation behavior of the low-alloy content Al–Zn–Mg aluminum alloys during subsequent artificial aging and related mechanisms, *Mater. Sci. Eng. A* 891 (2024) 145954, <https://doi.org/10.1016/j.msea.2023.145954>.
- [50] J. Mayer, L.A. Giannuzzi, T. Kamino, J. Michael, TEM sample preparation and damage, *MRS Bull.* 32 (2007) 400–407.
- [51] M.D. Abramoff, P.J. Magalhães, S.J. Ram, Image processing with ImageJ, *Biophotonics Int.* 11 (2004) 36–42.
- [52] Z. Yu, H. Li, P. Cai, X. Fu, Z. Feng, L. Zhang, J. Wang, N. Xiao, Effect of aging route on the precipitation behavior and thermal stability of Al–Cu–Mg–Ag alloy, *J. Mater. Res. Technol.* 23 (2023) 2010–2019, <https://doi.org/10.1016/j.jmrt.2023.01.140>.
- [53] Y. Li, Z. Liu, S. Bai, X. Zhou, H. Wang, S. Zeng, Enhanced mechanical properties in an Al–Cu–Mg–Ag alloy by duplex aging, *Mater. Sci. Eng. A* 528 (2011) 8060–8064, <https://doi.org/10.1016/j.msea.2011.07.055>.
- [54] J. Wang, J. Xie, Z. Mao, T. Liang, A. Wang, W. Wang, S. Hao, Microstructure evolution and mechanical properties of the Al–Cu–Mg–Ag alloy during non-isothermal aging, *J. Alloy. Compd.* 942 (2023) 169031, <https://doi.org/10.1016/j.jallcom.2023.169031>.
- [55] P.H. Miller Jr, J.W.M. DuMond, Tests for the validity of the X-ray crystal method for determining N and e with Aluminum, Silver and Quartz, *Phys. Rev.* 57 (1940) 198.
- [56] Y. Grin, F.R. Wagner, M. Armbrüster, M. Kohout, A. Leithe-Jasper, U. Schwarz, U. Wedig, H.G. von Schnering, CuAl₂ revisited: Composition, crystal structure, chemical bonding, compressibility and Raman spectroscopy, *J. Solid State Chem.* 179 (2006) 1707–1719.
- [57] J.T. Norton, H. Blumenthal, S.J. Sindeband, Structure of diborides of titanium, zirconium, columbium, tantalum and vanadium, *J. Miner. Met. Mater. Soc.* 1 (1949) 749–751, <https://doi.org/10.1007/BF03398932>.
- [58] J.K. Mackenzie, M.J. Thomson, Some statistics associated with the random disorientation of cubes, *Biometrika* 44 (1957) 205–210.
- [59] M.J. Starink, S.C. Wang, The thermodynamics of and strengthening due to co-clusters: General theory and application to the case of Al – Cu – Mg alloys, *Acta Mater.* 57 (2009) 2376–2389, <https://doi.org/10.1016/j.actamat.2009.01.021>.
- [60] K.S. Ghosh, Calorimetric studies of 2024 Al–Cu–Mg and 2014 Al–Cu–Mg–Si alloys of various tempers, *J. Therm. Anal. Calorim.* 136 (2019) 447–459, <https://doi.org/10.1007/s10973-018-7702-0>.
- [61] X.H. Zhu, Y.C. Lin, Q. Wu, Y.Q. Jiang, Effects of aging on precipitation behavior and mechanical properties of a tensile deformed Al–Cu alloy, *J. Alloy. Compd.* 843 (2020) 155975, <https://doi.org/10.1016/j.jallcom.2020.155975>.
- [62] Z. Chen, Y. Zhao, Z. Zhang, Theoretical and experimental study of precipitation and coarsening kinetics of θ' phase in Al–Cu alloy, *Vacuum* 189 (2021) 110263, <https://doi.org/10.1016/j.vacuum.2021.110263>.
- [63] C. García Cordovilla, E. Louis, Characterization of the microstructure of a commercial Al–Cu alloy (2 0 1 1) by differential scanning calorimetry (DSC), *J. Mater. Sci.* 19 (1984) 279–290, <https://doi.org/10.1007/BF02403136>.

- [64] K. Ma, H. Wen, T. Hu, T.D. Topping, D. Isheim, D.N. Seidman, E.J. Lavernia, J. M. Schoenung, Mechanical behavior and strengthening mechanisms in ultrafine grain precipitation-strengthened aluminum alloy, *Acta Mater.* 62 (2014) 141–155, <https://doi.org/10.1016/j.actamat.2013.09.042>.
- [65] S. Bai, X. Zhou, Z. Liu, P. Ying, M. Liu, S. Zeng, A Atom probe tomography study of Mg-dependent precipitation of Ω phase in initial aged Al-Cu – Mg – Ag alloys, *Mater. Sci. Eng. A.* 637 (2015) 183–188, <https://doi.org/10.1016/j.msea.2015.04.052>.
- [66] S. Bai, Z. Liu, P. Ying, J. Wang, A. Wang, Quantitative study of the solute clustering and precipitation in a pre- stretched Al-Cu-Mg-Ag alloy, *J. Alloy. Compd.* 725 (2017) 1288–1296, <https://doi.org/10.1016/j.jallcom.2017.07.258>.
- [67] S. Bai, H. Di, Z. Liu, Dislocation interaction with Ω phase in crept Al-Cu-Mg-Ag alloys, *Mater. Sci. Eng. A.* 651 (2016) 399–405, <https://doi.org/10.1016/j.msea.2015.10.031>.
- [68] J. da Costa Teixeira, D.G. Cram, L. Bourgeois, T.J. Bastow, A.J. Hill, C. R. Hutchinson, On the strengthening response of aluminum alloys containing shear-resistant plate-shaped precipitates, *Acta Mater.* 56 (2008) 6109–6122, <https://doi.org/10.1016/j.actamat.2008.08.023>.
- [69] J.F. Nie, B.C. Muddle, Strengthening of an Al-Cu-Sn alloy by deformation-resistant precipitate plates, *Acta Mater.* 56 (2008) 3490–3501, <https://doi.org/10.1016/j.actamat.2008.03.028>.
- [70] N. Hansen, Hall-petch relation and boundary strengthening, *Scr. Mater.* 51 (2004) 801–806, <https://doi.org/10.1016/j.scriptamat.2004.06.002>.
- [71] T. Shanmugasundaram, M. Heilmaier, B.S. Murty, V.S. Sarma, On the Hall-Petch relationship in a nanostructured Al-Cu alloy, *Mater. Sci. Eng. A.* 527 (2010) 7821–7825, <https://doi.org/10.1016/j.msea.2010.08.070>.
- [72] J.R. Davis, *Aluminum and Aluminum Alloys*, ASM International, 1993, <https://doi.org/10.1361/autb2001p351>.
- [73] T. Pardoen, D. Dumont, A. Deschamps, Y. Brechet, Grain boundary versus transgranular ductile failure, *J. Mech. Phys. Solids* 51 (2003) 637–665, [https://doi.org/10.1016/S0022-5096\(02\)00102-3](https://doi.org/10.1016/S0022-5096(02)00102-3).
- [74] G.M. Ludtka, D.E. Laughlin, The influence of microstructure and strength on the fracture mode and toughness of 7XXX series aluminum alloys, *Metall. Trans. A.* 13 (1982) 411–425, <https://doi.org/10.1007/BF02643350>.